

Absence of critical thickness in improper ferroelectric hexagonal-YbFeO₃ thin films

Xiaoshan Xu (✉ xiaoshan.xu@unl.edu)

University of Nebraska-Lincoln

Yu Yun

University of Nebraska-Lincoln

Pratyush Buragohain

University of Nebraska-Lincoln

Arashdeep Thind

Washington University in St. Louis <https://orcid.org/0000-0003-0262-766X>

Yuewei Yin

University of Nebraska-Lincoln

Xin Li

University of Nebraska-Lincoln

Xuanyuan Jiang

University of Nebraska-Lincoln

Rohan Mishra

Washington University in St. Louis <https://orcid.org/0000-0003-1261-0087>

Alexei Gruverman

University of Nebraska-Lincoln <https://orcid.org/0000-0003-0492-2750>

Physical Sciences - Article

Keywords: improper ferroelectrics, hexagonal-YbFeO₃, ferroelectric/dielectric bilayer structures, scalable thin-film device applications

Posted Date: September 9th, 2020

DOI: <https://doi.org/10.21203/rs.3.rs-69694/v1>

License:  This work is licensed under a Creative Commons Attribution 4.0 International License.

[Read Full License](#)

Absence of critical thickness in improper ferroelectric hexagonal-YbFeO₃ thin films

Yu Yun¹†, Pratyush Buragohain¹†, Arashdeep Singh Thind², Yuewei Yin¹, Xin Li¹, Xuanyuan Jiang¹, Rohan Mishra^{2,3}, Alexei Gruverman¹, Xiaoshan Xu^{1,4*}

¹Department of Physics and Astronomy, University of Nebraska, Lincoln, Nebraska 68588, USA

²Institute of Materials Science & Engineering, Washington University in St. Louis, St. Louis MO, USA

³Department of Mechanical Engineering & Materials Science, Washington University in St. Louis, St. Louis MO, USA

⁴Nebraska Center for Materials and Nanoscience, University of Nebraska, Lincoln, Nebraska 68588, USA

†Joint first authors

Abstract

Improper ferroelectrics are highly promising for technological applications due to their expected persisting polarizations even at ultrathin limits. However, the evolution of their electrical behaviors with thickness, including the magnitude of the polarization and the switching mechanism, remain unresolved experimentally. This is primarily due to the difficulty in growth and characterization of ultrathin improper ferroelectric films. Here, we investigated the spontaneous polarization and switching mechanism in ferroelectric/dielectric bilayer structures, which allows the decoupling of the electrostatic and interfacial effects and circumventing the need for ultrathin films. We show that, for the bilayer structures of prototypical improper ferroelectrics h-YbFeO₃ and dielectrics CoFe₂O₄, although the effective spontaneous polarization is significantly reduced by the dielectric layer due to the electrostatic under-screening, it persists at least down to a ferroelectric/dielectric thickness ratio of about 2, with no evidence of critical thickness. Interfacial clamping that suppresses the primary structural distortion of h-YbFeO₃ have been observed, which appears to play an important role in ferroelectric domain pinning. The microstructure caused by the heteroepitaxy favors a nucleation-limited polarization switching dynamics. These results demonstrate the much-desired absence of critical thickness in improper ferroelectrics for the scalable thin-film device applications; they also reveal significant impact of the mismatched film/substrate epitaxy on the polarization switching mechanism.

Introduction

Ferroelectric materials exhibit an electrically switchable spontaneous polarization. Their advantageous electrical, thermal, and optical properties enable critical applications in sensors, actuators, resonators, detectors, optical switches, and non-volatile memory devices^{1,2}. A well-known limiting factor is the critical thickness, below which ferroelectricity is suppressed by the electrostatic energy, as a result of the finite screening length of the electrodes and the presence of the non-ferroelectric interfacial layer³⁻⁵.

Presumably, this long-standing problem of the critical thickness could be alleviated in improper ferroelectrics, where the spontaneous polarization emerges indirectly from the primary non-polar structural distortion that breaks the inversion symmetry and induces a polar distortion as a byproduct^{6,7}. The secondary nature of improper ferroelectricity makes the primary structural distortion impervious to electrostatic depolarization effects, i.e. no critical thickness for the occurrence of the primary structural distortion is expected^{6,7}, making improper ferroelectrics more appealing for scalable electronic devices. Indeed, a previous work on epitaxial thin films of the prototypical improper ferroelectric, hexagonal YMnO₃, has demonstrated that the primary non-polar K₃ structural distortion persists down to a thickness of two unit cells, which is attributed to the interfacial clamping effect that suppresses the primary structural distortion due to the film/substrate structural mismatch⁸.

However, although the electrostatic effects may not quench the primary structural distortion, their effects on the spontaneous polarization have not been properly addressed. In addition, an understanding of the polarization switching mechanism is of vital importance for any technological applications^{9,10}. The difficulty in growth and electrical characterization of ultrathin films on structurally mismatched substrates, coupled with the intertwined interfacial and electrostatic effects, might have contributed to the lack of systematic studies in this regard.

In this work, we have designed an ferroelectric/dielectric bilayer structure, with h-YbFeO₃ as the improper ferroelectric and CoFe₂O₄ as the dielectric. The length scale of the electrostatic depolarization effect is determined by the thickness of the dielectric layer, allowing one to separate the electrostatic and the interfacial effects. We show that indeed there is no evidence of critical thickness; in addition, the microstructure originated from film/substrate structural mismatch has a substantial impact on the effective spontaneous polarization and the polarization switching mechanism.

Results

The heterostructure Au/h-YbFeO₃/CoFe₂O₄/La_{0.67}Sr_{0.33}MnO₃ (Au/h-YbFeO₃/CFO/LSMO) studied in this work is shown in Fig. 1a. The (111)-oriented LSMO bottom electrode was grown on SrTiO₃ (STO) (111) substrate. The (111)-oriented CFO dielectric layer (10 - 18 nm) is used to tune the electrostatic energy of the ferroelectric/dielectric (FE/DE) bilayer sandwiched between the electrodes. The CFO layer also serves as a buffer that effectively reduces the lattice mismatch between the LSMO and the h-YbFeO₃ layers as shown in Table S1 (see Supplementary Material Section 1). Improper ferroelectric h-YbFeO₃, which is isomorphic with h-YMnO₃, has a layered hexagonal structure with the $P6_3cm$ space group, as shown in Fig. 1b (left). The direction of the polar Γ_2^- structural distortion and the corresponding spontaneous polarization P are determined by the angle of the K₃ structural distortion Φ which can be integer times $\pi/3$ ¹¹, as indicated in Fig.

1b (right) using the displacement pattern of the oxygen atoms above the Fe atoms in the top view of the Fe local environments.

To investigate the electrostatic effect of the DE layer on the spontaneous polarization of the FE layer, we first note that because of the dielectric layer, the polarization P of the ferroelectric layer does not have the same magnitude as the area density of the screening charge σ on the electrodes (Fig. 1c). In addition, the screening charge σ is actually what is being measured in the experiments and can be viewed as the effective polarization of the FE/DE bilayer. We have measured the hysteretic relation between σ and voltage (V) across the FE/DE bilayer at 500 Hz for various FE/DE thickness ratio (t_F/t_D), where t_F and t_D are the thicknesses of the h-YbFeO₃ and CFO layers, respectively. As shown in Fig. 1d, at 20 K, with the non-switching background subtracted using the PUND (positive-up-negative-down) method¹² (see also Supplementary Material Section 2), the $\sigma - V$ loop changes dramatically with the thickness ratio t_F/t_D , where t_D is fixed around 10 nm. In particular, as shown in Fig. 1e, the remanence σ_r increases with t_F/t_D and saturates for $t_F/t_D \approx 8.5$ at a level of $\sim 8.4 \mu\text{C}/\text{cm}^2$. This is consistent with previous observations and theoretical calculations for hexagonal ferrites and manganites¹³⁻¹⁵. In addition, there appears to be a transition around $t_F = 40$ nm ($t_F/t_D \approx 4$), at which a rapid reduction of σ_r is observed (Fig. 1e). Two mechanisms might be responsible for the observed reduction in σ_r in thinner films: the reduction of the magnitude of the primary K₃ structural distortion (Q) that induces the polarization, and the electrostatic under-screening.

To elucidate the possibility of reduced K₃ structural distortion and characterize the crystal structure of the h-YbFeO₃/CFO interface and the h-YbFeO₃ film, we have carried out atomic scale imaging using aberration-corrected scanning transmission electron microscopy (STEM) imaging. Fig. 2a shows a wide field of view cross-sectional high-angle annular dark field (HAADF) image of the h-YbFeO₃/CFO/LSMO/STO (111) heterostructure. We observe epitaxial growth for each layer in the films; the thicknesses of all the layers are consistent with the fitting results of X-ray reflection (XRR) (see Supplementary Material Section 1). Atomic resolution HAADF-STEM image for the interface between the h-YbFeO₃ layer and the CFO layer, viewed along h-YbFeO₃ [100] zone axis, is shown in Fig. 2b. The crystal structural model for the interface is shown in Fig. 2c. Both CFO [-211] // h-YbFeO₃ [100] and CFO [-211] // h-YbFeO₃ [1-10] (see Supplementary Material Section 1) interfaces are identified using STEM. The CFO [-211] // h-YbFeO₃ [1-10] in-plane epitaxial relation is consistent with the observed reflection high energy electron diffraction (RHEED) patterns (see Supplementary Material Section 1), which is similar to that of the previously reported h-LuFeO₃ (001) / Fe₃O₄ (111) epitaxial interface¹⁶.

In the HAADF imaging mode, electrons elastically scattered at high angles are collected by an annular detector from each point (pixel) as the beam rasters through the sample. As a result, the intensity in an HAADF image of an atomic column is approximately proportional to the squared atomic number ($\sim Z^2$)¹⁷. As shown in Fig. 2b, Yb atoms ($Z = 70$) appear brightest, where the vertical displacement pattern of the Yb atoms, either “two-up-one-down” or “one-up-two-down”, and hence, the polarization direction can be mapped. Domains with opposing polarization direction and the corresponding domain walls are shown in Fig. 2b. As illustrated in Fig. 1b, the buckling of the Yb layer is a key aspect of the atomic displacement of the K₃ structural distortion; it is expected that the vertical displacement of the Yb atoms from the buckling is proportional to the magnitude of the K₃ structural distortion^{8,18}. The magnitude of the primary K₃ structural

distortion can be extracted from the arrangement of the Yb atoms. Fig. 2d shows an atomically resolved HAADF-STEM image, where the FE polarization in the h-YbFeO₃ film is pointing up. Based on the HAADF intensities, we can determine the position of the Yb atoms (brightest) and calculate the average vertical displacement. A part of the HAADF-STEM image in Fig. 2d is overlaid with the determined positions of the Yb atoms. The average vertical displacement $|\langle Q' \rangle|$ of Yb atoms extracted from Fig. 2d is plotted against the distance from the interface [see Ref. ^{8,18} for definition], as shown in Fig. 2e. These displacements are compared with that obtained at the film/substrate interface for h-YMnO₃ and h-LuFeO₃ films from literature. For all the film/substrate combinations, such as h-LuFeO₃/YSZ (yttria-stabilized cubic zirconia) ¹⁹, h-YMnO₃/YSZ ⁸, and h-YMnO₃/Al₂O₃ ²⁰, the interfacial clamping effects are clear since the magnitude of K₃ structural distortion are significantly suppressed at all the interfaces ⁸. Although the depth of the clamping effect varies, the magnitude of K₃ structural distortion saturates within two unit cells (four rare-earth layers) from the interface. Hence, this limited influence of substrate clamping on the magnitude of K₃ structural distortion is unlikely the origin of the reduction in σ_r since the latter occurs at a length scale far above 2.4 nm (thickness of two unit cells).

Therefore, it is most likely that the thickness dependence of σ_r observed in Fig. 1d is coming from electrostatic under-screening due to the dielectric layer, which can be modeled as in the following. As illustrated in Fig. 1c, ignoring the interfacial effects, it can be derived that (see the Supplementary Material Section 4)

$$P = \frac{\varepsilon_0 V}{t_F} - \sigma \left(1 + \frac{\varepsilon_0 t_D}{\varepsilon_D t_F} \right), \quad (1)$$

where ε_0 and ε_D are the permittivity of vacuum and the dielectric material, respectively. The negative sign in front of σ is a reminder that the charge density on the electrodes is to “screen” the bound charges on the ferroelectric layer. Under the short-circuit condition ($V = 0$), the remanence follows $|\sigma_r| < |P_r|$, corresponding to the under-screening; the ratio $|\sigma_r|/|P_r|$ increases with t_F/t_D and saturates at 1 when $t_F/t_D \rightarrow \infty$. The under-screening leads to a non-zero electric field (voltage gradient) in both the ferroelectric and the dielectric layers even under the short-circuit condition (Fig. 1c), which is the source of the electrostatic energy that leads to the critical thickness of the proper ferroelectrics ²¹. Eq. (1) holds for both proper ^{3,5,22} and improper ferroelectrics since it does not specify the dependence of P and σ on V .

To find the $P - V$ and $\sigma - V$ relations and to understand how the under-screening affects P and σ in improper ferroelectrics, we carry out a Landau-theory analysis (see Supplementary Material Section 4) ¹¹. By minimizing the Gibbs free energy with respect to P , we reach a linear relation between P and V :

$$P = \frac{C_{VF} + C_D}{C_D + C_F} P_{r0} - \frac{1}{1 + \frac{C_F}{C_D}} \frac{P_{r0}}{E_{C0}} \frac{V}{t_F}, \quad (2)$$

where P_{r0} and E_{C0} are the remanent polarization and static-switching coercive field without the dielectric layer respectively, $C_{VF} \equiv \frac{A\varepsilon_0}{t_F}$ and C_F are the vacuum and effective capacitance of the ferroelectric layer, $C_D \equiv \frac{A\varepsilon_D}{t_F}$ is the capacitance of the dielectric layer, A is the area of the capacitor (see Supplementary Material Section 4). According to Eq. (2), the dielectric layer has only a limited effect on the remanence P_r , since even when C_D approaches 0 ($t_D \rightarrow \infty$, completely

unscreened), P_r is reduced to the finite value $\frac{C_{VF}}{C_F} P_{r0}$. This suggests that there is no critical thickness at which P_r drops to zero due to the under-screening.

In contrast, the under-screening has a much larger effect on the effective polarization σ . Plugging Eq. (2) into Eq. (1), one finds another linear relation between σ and V :

$$\sigma = \frac{1}{1 + \frac{C_F}{C_D}} \left(\sigma_{r0} + \frac{C_F V}{A} \right), \quad (3)$$

where $\sigma_{r0} = -P_{r0}$. When C_D approaches 0 ($t_D \rightarrow \infty$), the remanence $\sigma_r = \frac{\sigma_{r0}}{1 + \frac{C_F}{C_D}}$ vanishes corresponding to the complete unscreened polarization (no screening charge). The thickness dependence of σ_r can be written as

$$\sigma_r \left(\frac{t_F}{t_D} \right) = \frac{\sigma_{r0}}{1 + \frac{C_F \epsilon_0 t_D}{C_{VF} \epsilon_D t_F}} \quad (4)$$

Recall that in Fig. 1e, two different trends were found for the σ_r dependence on t_F/t_D . We fit the experimental $\sigma_r(t_F/t_D)$ relation for $t_F/t_D > 5$ using Eq. (4), the fitting curve is plotted in Fig. 1e as the dashed line. We find that $|P_{r0}|$ is about $10.9 \pm 0.1 \mu\text{C}/\text{cm}^2$, which is in fair agreement with the theoretical value 9.6 for h-YbFeO₃¹⁵. The factor $\frac{C_F \epsilon_0}{C_{VF} \epsilon_D}$ was found to be 2.60 ± 0.07 .

The apparent transition at around 40 nm in Fig. 1e, however, cannot be explained by the above analysis. Significant reduction due to the interfacial clamping effect is also unlikely considering the 40-nm length scale. To confirm the nature of the effect, we studied another sequence of samples with fixed thickness (~ 38 nm) of the h-YbFeO₃ layer and various CFO layer thicknesses. As shown in Fig. 1e, the results (blue squares) appear to scale with the t_F/t_D ratio, suggesting that the sudden reduction of σ_r at around 40 nm is related to the electrostatic energy and under-screening. One possibility is that at small t_F/t_D , the enhanced electrostatic energy overcomes the cost of domain-wall energy, triggering the formation of multidomain structure to reduce the total energy. Experimental evidence of multiple domains can be found in a 44-nm h-YbFeO₃ film in Fig. 2b. Below, we investigate the mechanism in more detail.

In the FE/DE bilayer capacitor structures, the electrostatic energy density from the under-screened electric field increases as t_F/t_D decreases, which leads to the formation of multiple domains to reduce the electrostatic energy at the cost of domain-wall energy. The maximum domain size is also limited by the grain size of the films, which was found to be around 10 nm in film samples studied in this work (see Supplementary Material Section 1). This small size comes from the unavoidable structural anti-phase boundaries (APBs) in epitaxial thin films, which could be attributed to the difference in in-plane unit cell sizes between the film and substrate, the steps at the interface and the defects of buffer layer (see Supplementary Material Section 1). The formation of multi domains in small grains exhibits a small domain-wall energy density. Previous work found that the domain wall energy density is much smaller in hexagonal manganites than in other proper ferroelectrics²³, due to the possible frustration-free structure of the domain wall. Hexagonal ferrites, isomorphic to hexagonal manganites, is also expected to be similar. For a more quantitative analysis, we compared the Gibbs free energies of the single domain and multidomain cases (See supplementary Material Section 4). At the single-multi domain transition, these two Gibbs free energies are equal, which requires

$$\left(\frac{s_Q \pi^2}{9} Q^2\right) \frac{1}{w_D D} = \frac{\varepsilon_0 + \varepsilon_D}{\left(\varepsilon_0 + \varepsilon_D + \varepsilon_D \frac{D}{t_D} + \varepsilon_0 \frac{D}{t_F}\right) \left(\varepsilon_0 + \varepsilon_D \frac{t_F}{t_D}\right)} P^2, \quad (5)$$

where s_Q and w_D are the stiffness and width of the domain wall, respectively, and D is the length of the ferroelectric domain.

Using Eq. (5), one may estimate the wall stiffness s_Q . Plugging the values $w_D = 0.5$ nm¹¹, $D = 10$ nm, $t_F = 40$ nm, $t_D = 10$ nm and $\varepsilon_D/\varepsilon_0 = 14$ ²⁴, $Q = 0.1$ nm, $P = 10$ $\mu\text{C}/\text{cm}^2$ in Eq. (5), one finds $s_Q \approx 2 \times 10^9$ J/m³ (5 eV per unit cell), consistent with the value found previously in h-YMnO₃ from first-principles calculations¹¹.

Therefore, we have elucidated the effective spontaneous polarization σ_r of the FE/DE bilayer capacitor structure, in terms of the characteristics of the film samples such as under-screening, interfacial clamping, and microstructure (grain size): While σ_r decreases monotonically as t_F/t_D decreases due to the under-screening, no evidence of critical thickness was found. The reduction of σ_r induced by the formation of multi domains is also tuned by the grain size of the films. The interfacial clamping appears to play an unimportant role here on the magnitude of polarization. Next, we study the polarization switching mechanism and identify the role of interface, microstructure, and under-screening.

To elucidate the physical process of polarization switching, we note that the spontaneously poled ferroelectrics can be treated as a system in a potential well; the static switching corresponds to the toppling of the potential well by an external electric field. The threshold electric field needed for static switching is expected to decrease because of under-screening, since it tends to destabilize the spontaneous polarization (see Supplementary Material Section 4). On the other hand, experimental observation indicates that the average coercive field $E_c \equiv (E_c^+ - E_c^-)/2$ decreases with t_F/t_D (Fig. 1e, inset), which is opposite for the expected trend from switching tuned by the under-screening. Therefore, the switching is more likely governed by the domain nucleation and domain wall motion. The thickness dependence of E_c can be fitted using a power law $E_c \propto 1 + d_0 t_F^n$, where the $d_0 \approx 822$ nm⁻¹ and $n \approx -0.99$ are found. The $n \approx -0.99$ value suggests a strong interfacial pinning effect. As discussed by Tagantsev²⁵, the external electric field is needed to overcome the pinning of the domain wall, which, in a thin film, can be divided into the inner and surface parts²⁶. When the surface part contributes significantly, an inverse dependence of E_c on the film thickness discussed above is expected. The interfacial clamping found in Fig. 2 could well be the origin of the surface pinning. In addition, as shown in Fig. 1d, asymmetry of the $\sigma - V$ loops was observed, which could be attributed to the asymmetric capacitor structure. This asymmetry is enhanced for small t_F/t_D (see also Supplementary Material Section 2), highlighting its interfacial origin.

Finally, the polarization switching dynamics was investigated in the h-YbFeO₃ film of $t_{\text{YbFO}}/t_{\text{CFO}} \sim 3.1$ at room temperature. The polarization switching dynamics in proper ferroelectrics can be broadly described by either the Kolmogorov-Avrami-Ishibashi (KAI)²⁷ model in which the limiting parameter is the domain wall velocity, or the nucleation limited switching (NLS) model,²⁸ in which the limiting parameter is the nucleation time for new domains. First, remnant $\sigma - V$ loops were collected as a function of the measurement frequency (Fig. 3a) using the PUND technique (in Fig.S11(a), see Supplementary Material Section 3) to subtract any non-switching contribution to the measured σ . The increase in the measurement frequency leads to an increase in the coercive field, which is well-known in proper ferroelectrics. In the context of the frequency

dependence of coercive fields, Ishibashi and Orihara extended the KAI model to obtain a power law, $E_c \sim f^\beta$, where E_c is the coercive field and f is the measurement frequency²⁹; while, based on a nucleation-controlled mechanism, Du and Chen obtained a logarithmic dependence of E_c with f : $\ln(f) = \ln(f_0) + \alpha/E_c^2$, where f_0 is the cutoff frequency³⁰. Here, the average coercive field E_c is plotted as a function of the frequency in Fig. 3(b) and fit with the two aforementioned models. The fitting with the power law gave the value of the exponent, $\beta = 0.28$, which is higher than that reported in h-ErMnO₃ bulk single crystals ($\beta \approx 0.1$)⁹ but lower than the value reported in h-LuFeO₃ thin films ($\beta \approx 0.66$)¹⁰. On the other hand, from the Du-Chen model, a cutoff frequency of ~ 365 kHz was obtained which is lower than that in PZT thin films (1~2 MHz)³¹, but similar to that in barium strontium titanate (BST) thin films³². As mentioned in Ref. ³¹, the cutoff frequency is dependent on the capacitor area, and the ratio of the capacitor areas used in our study and that used in Ref. ³² for BST thin films are ~ 1.17 , which might explain the similarity in the cutoff frequencies. From these fits, it appears that both these two models can describe the switching mechanism at room temperature. Such a scenario was reported earlier in proper ferroelectric thin films where the authors of that study resolved this ambiguity by performing temperature dependent E_c vs f measurements³². Another possible way of resolving this ambiguity without resorting to temperature dependent measurements is using square pulses in the manner described by Tagantsev and co-workers²⁸, which is discussed below.

The square-pulse waveform used to investigate the polarization switching dynamics at room temperature is shown in Fig. S11(b) (see Supplementary material Section 3). The switched polarization as a function of the pulse duration for different applied voltages using the above procedure is shown in Fig. 3c, which has been fitted by the following equation²⁸:

$$\Delta P(t) = 2P_S \int_{-\infty}^{\infty} \left[1 - \exp\left\{-\left(\frac{t}{t_0}\right)^n\right\}\right] \cdot F(\log t_0) \cdot d(\log t_0) \quad (6)$$

where $n=2$ (for thin films) was used, and $F(\log t_0)$ is the distribution function of the characteristic switching time (t_0). For the Kolmogorov-Avrami-Ishibashi (KAI) model²⁷, $F(\log t_0)$ is a Dirac-delta function, while, for the NLS model³³, it is a Lorentzian function given by

$$F(\log t_0) = \frac{A}{\pi} \left[\frac{w}{(\log t_0 - \log t_l)^2 + w^2} \right] \quad (7)$$

where A is a normalization constant, w is the half width at half-maximum, and $\log t_l$ is the central value of the distribution. The inset of Fig. 3c shows the corresponding distribution functions in the fitting of NLS model associated with different applied voltages. The representative fitting results with respect to the different models are shown in Fig. 3d. The red line and blue line indicate the fitting results using NLS model and KAI model, respectively, in Fig. 3d. It was found that the fitting curve with the KAI model cannot adequately describe the experimental data, especially for the slow part of the switching curve. The NLS model with the Lorentzian distribution gives the best fit to describe the switching process.

In case of single crystals with topologically protected domain patterns³⁴, it was reported that domains of the preferential polarization state expand while that for the opposite polarization state shrink^{34,35}, highlighting the important role played by the domain walls during electrical polarization reversal. This scenario was essentially verified by Ruff *et al* who found that the β -exponent value in their h-ErMnO₃ single crystals matched very well with proper ferroelectrics undergoing polarization reversal purely through domain wall motion⁹. However, the situation might be drastically different in thin films with a high percentage of defects and/or small grain

size. Both factors can severely restrict the movement of the domain walls such that the mechanism of polarization reversal changes to the nucleation limited one. The obtained β -exponent value of ~ 0.28 in our films is about three times that of the value obtained by Ruff *et al* for pure domain wall motion. For the proper ferroelectrics, such as poly-crystalline PZT^{28,33} and doped poly-crystalline HfO₂ films^{36,37}, which can be considered as an ensemble of regions that switch independently of each other, it was shown that the NLS model could best describe the switching mechanism. Given that our h-YbFeO₃ films are composed of nanometer size grains, it can be assumed that their switching behavior is also governed by the NLS mechanism. In addition, surface pinning effects can also further restrict the motion of domain walls.

Therefore, microstructure-related nucleation process and the surface pinning are critical for the polarization switching process. In contrast, the polarization switching is not obviously affected by the under-screening.

Conclusions

Using a FE/DE bilayer capacitor structure, we have demonstrated that in improper ferroelectric h-YbFeO₃ spontaneous polarization persists down to small FE/DE layer thickness ratio ($t_F/t_D \approx 2$) despite the significant reduction from the bulk value due to the under-screening. Therefore, no critical thickness is expected for improper ferroelectrics. On the other hand, the structural clamping that quenches the interfacial primary distortion may put a lower limit of thickness for ferroelectricity at around 1 nm. The interfacial clamping as well as the finite crystal grain size caused by the heteroepitaxy, play much more important roles in polarization switching dynamics. These results provide an important insight into the fundamental properties of improper ferroelectrics and offer critical guidance for the design of miniaturized devices using ultrathin improper ferroelectric thin films.

Methods

Sample deposition and preparation. The h-YbFeO₃/CFO epitaxial thin films were grown on LSMO-buffered STO (111) substrates using pulsed laser deposition (PLD) with base pressure lower than 3×10^{-7} mTorr, a repetition rate of 2 Hz. Before the deposition, the substrates were pre-annealed at 700 °C for 1 hour. During the growth, the substrate temperature was kept at 700 °C, 600 °C and 700 °C - 920 °C for LSMO, CFO and h-YbFeO₃ layer, respectively. The growth oxygen pressures, during the growth of LSMO, CFO and h-YbFeO₃ layers, are 80 mTorr, 10 mTorr and 10 mTorr, respectively. The Au (~ 10 nm) top electrodes were evaporated by an AJA sputtering system with 200 - 400 μm diameter.

Structural characterization. The in-situ RHEED was used to monitor the growth of the thin films. The crystal structure of the epitaxial films, the rocking curves, and the thickness of heterostructures were measured by XRD (Rigaku SmartLab Diffractometer). The typical thicknesses of LSMO and CFO layers are ~ 30 nm and ~ 10 nm, respectively. The thin-film topography was characterized using atomic force microscopy (AFM, Bruker Dimension ICON SPM).

Ferroelectric characterization. The ferroelectric properties are measured using RT66C Radiant Ferroelectric Tester. For the measurements of the polarization switching dynamics, the voltage pulses were applied using a Keysight 33621A arbitrary waveform generator while the transient switching currents were recorded by a Tektronix TDS 3014B oscilloscope. In all measurements, the bias was applied to the top electrode (diameter from 200 μm to 400 μm) while the bottom electrode was grounded. The low-temperature measurements are implemented using Cryostat, Sumitomo Cryogenics.

High-resolution electron microscopy. Scanning transmission electron microscopy (STEM) imaging was carried out using the aberration corrected Nion UltraSTEM™ 200 microscope (operating at 200 kV) at Oak Ridge National Laboratory. This microscope is equipped with a fifth-order aberration corrector and a cold-field emission electron gun. A thin foil for STEM characterization was prepared using a Hitachi NB5000 focused ion and electron beam system. The top of the film was coated with a 1- μm -thick layer of carbon to protect against ion beam damage. A 20 kV beam with 0.7 nA current was used to cut the lift-out. Rough and fine milling were performed using beam currents of 0.07 nA at 10 kV and 0.01 nA at 5 kV to make the foil electron transparent. The resulting foil was mounted on a Cu grid for scanning transmission electron microscopy (STEM) experiments. The Cu grid was baked at 160 $^{\circ}\text{C}$ under vacuum prior to the STEM experiments to remove surface impurities.

Data availability

The datasets generated during and/or analysed during the current study are available from the corresponding author on reasonable request.

Acknowledgements

This work was primarily supported by the National Science Foundation (NSF), Division of Materials Research (DMR) under Grant No. DMR-1454618. The research was performed in part in the Nebraska Nanoscale Facility: National Nanotechnology Coordinated Infrastructure and the Nebraska Center for Materials and Nanoscience, which are supported by the NSF under Grant No. ECCS-1542182, and the Nebraska Research Initiative. Work at Washington University was supported by NSF Grant No. DMR-1806147. STEM experiments were conducted at the Center for Nanophase Materials Sciences at Oak Ridge National Laboratory, which is a Department of Energy (DOE) Office of Science User Facility, through a user project.

Author Contributions

The thin films were synthesized by Y.Y. with the assistance from X.X. and Y.Y. in. Crystal structure and low-temperature ferroelectric properties were characterized by Y.Y. STEM experiments were performed by A.S.T under the supervision of R.M., and analysis was performed by A.S.T., R.M. and X.L. The ferroelectric switching mechanisms were measured by P.B. under the supervision of A.G. X.X. developed the phenomenological theory. Y.Y. and X.X. wrote the manuscript. The study was conceived and guided by X.X. All authors discussed results and commented on the manuscript.

Author Information

The authors declare no competing financial interests. Readers are welcome to comment on the online version of the paper. Correspondence and requests for materials should be addressed to X.X. (xiaoshan.xu@unl.edu).

References:

- 1 Setter, N. *et al.* Ferroelectric thin films: Review of materials, properties, and applications. *J. Appl. Phys.* **100**, 051606 (2006).
- 2 Scott, J. F. Applications of Modern Ferroelectrics. *Science* **315**, 954-959 (2007).
- 3 Rault, J. E. *et al.* Thickness-Dependent Polarization of Strained BiFeO₃ Films with Constant Tetragonality. *Phys. Rev. Lett.* **109**, 267601 (2012).
- 4 Fong, D. D. *et al.* Ferroelectricity in ultrathin perovskite films. *Science* **304**, 1650-1653 (2004).
- 5 Junquera, J. & Ghosez, P. Critical thickness for ferroelectricity in perovskite ultrathin films. *Nature* **422**, 506-509 (2003).
- 6 Stengel, M., Fennie, C. J. & Ghosez, P. Electrical properties of improper ferroelectrics from first principles. *Phys. Rev. B* **86**, 094112 (2012).
- 7 Sai, N., Fennie, C. J. & Demkov, A. A. Absence of critical thickness in an ultrathin improper ferroelectric film. *Phys. Rev. Lett.* **102**, 107601 (2009).
- 8 Nordlander, J. *et al.* The ultrathin limit of improper ferroelectricity. *Nat. Commun.* **10**, 5591 (2019).
- 9 Ruff, A. *et al.* Frequency dependent polarisation switching in h-ErMnO₃. *Appl. Phys. Lett.* **112**, 182908 (2018).
- 10 Barrozo, P. *et al.* Defect-Enhanced Polarization Switching in the Improper Ferroelectric LuFeO₃. *Adv. Mater.* **32**, 2000508 (2020).
- 11 Artyukhin, S., Delaney, K. T., Spaldin, N. A. & Mostovoy, M. Landau theory of topological defects in multiferroic hexagonal manganites. *Nat. Mater.* **13**, 42-49 (2014).
- 12 Fukunaga, M. & Noda, Y. New Technique for Measuring Ferroelectric and Antiferroelectric Hysteresis Loops. *J. Phys. Soc. Jpn.* **77**, 064706 (2008).
- 13 Smolenskii, G. A. & Bokov, V. A. Coexistence of Magnetic and Electric Ordering in Crystals. *J. Appl. Phys.* **35**, 915-918 (1964).
- 14 Van Aken, B. B., Palstra, T. T. M., Filippetti, A. & Spaldin, N. A. The origin of ferroelectricity in magnetoelectric YMnO₃. *Nat. Mater.* **3**, 164-170 (2004).
- 15 Das, H., Wysocki, A. L., Geng, Y., Wu, W. & Fennie, C. J. Bulk magnetoelectricity in the hexagonal manganites and ferrites. *Nat. Commun.* **5**, 2998 (2014).
- 16 Zhang, X., Yin, Y., Yang, S., Yang, Z. & Xu, X. Effect of interface on epitaxy and magnetism in h-RFeO₃/Fe₃O₄/Al₂O₃ films (R = Lu, Yb). *J. Phys. Condens. Matter* **29**, 164001 (2017).
- 17 Jesson, S. J. P. a. D. E. High-resolution Z-contrast imaging of crystals. *Ultramicroscopy* **37**, 14-38 (1991).
- 18 Holtz, M. E. *et al.* Topological Defects in Hexagonal Manganites: Inner Structure and Emergent Electrostatics. *Nano Lett.* **17**, 5883-5890 (2017).
- 19 Wang, W. *et al.* Visualizing weak ferromagnetic domains in multiferroic hexagonal ferrite thin film. *Phys. Rev. B* **95**, 134443 (2017).
- 20 Cheng, S. *et al.* Interface reconstruction with emerging charge ordering in hexagonal manganite. *Sci. Adv.* **4**, eaar4298 (2018).
- 21 Íñiguez, J., Zubko, P., Luk'yanchuk, I. & Cano, A. Ferroelectric negative capacitance. *Nat. Rev. Mater.* **4**, 243-256 (2019).
- 22 Kim, Y. S. *et al.* Critical thickness of ultrathin ferroelectric BaTiO₃ films. *Appl. Phys. Lett.* **86**, 102907 (2005).

- 23 Kumagai, Y. & Spaldin, N. A. Structural domain walls in polar hexagonal manganites. *Nat. Commun.* **4**, 1540 (2013).
- 24 Gutierrez, D. *et al.* Dielectric response of epitaxially strained CoFe_2O_4 spinel thin films. *Phys. Rev. B* **86**, 125309 (2012).
- 25 Tagantsev, A. K. Size effects in polarization switching in ferroelectric thin films. *Integr. Ferroelectr.* **16**, 237-244 (1997).
- 26 Callaby, D. R. Domain Wall Velocities and the Surface Layer in BaTiO_3 . *J. Appl. Phys.* **36**, 2751-2760 (1965).
- 27 Yoshihiro Ishibashi, Y. T. Note on Ferroelectric Domain Switching. *J. Phys. Soc. Jpn.* **31**, 506-510 (1971).
- 28 Tagantsev, A. K., Stolichnov, I., Setter, N., Cross, J. S. & Tsukada, M. Non-Kolmogorov-Avrami switching kinetics in ferroelectric thin films. *Phys. Rev. B* **66**, 214109 (2002).
- 29 Ishibashi, Y. & Orihara, H. A theory of D-E hysteresis loop. *Integr. Ferroelectr.* **9**, 57-61 (1995).
- 30 Chen, X. D. a. I.-W. Frequency Spectra of Fatigue of PZT and other Ferroelectric Thin Films. *MRS Online Proc. Libr.* **493**, 311-316 (1997).
- 31 Takaakitsurumi, Num, S.-M., Kil, Y.-B. & Wada, S. High frequency measurements of P-E hysteresis curves of PZT thin films. *Ferroelectrics* **259**, 43-48 (2001).
- 32 Jung, D. J., Dawber, M., Scott, J. F., Sinnamon, L. J. & Gregg, J. M. Switching Dynamics in Ferroelectric Thin Films: An Experimental Survey. *Integr. Ferroelectr.* **48**, 59-68 (2010).
- 33 Jo, J. Y. *et al.* Domain switching kinetics in disordered ferroelectric thin films. *Phys. Rev. Lett.* **99**, 267602 (2007).
- 34 Choi, T. *et al.* Insulating interlocked ferroelectric and structural antiphase domain walls in multiferroic YMnO_3 . *Nat. Mater.* **9**, 253-258 (2010).
- 35 Jungk, T., Hoffmann, Á., Fiebig, M. & Soergel, E. Electrostatic topology of ferroelectric domains in YMnO_3 . *Appl. Phys. Lett.* **97**, 012904 (2010).
- 36 Mulaosmanovic, H. *et al.* Switching Kinetics in Nanoscale Hafnium Oxide Based Ferroelectric Field-Effect Transistors. *ACS Appl. Mater. Interfaces* **9**, 3792-3798 (2017).
- 37 Buragohain, P. *et al.* Nanoscopic studies of domain structure dynamics in ferroelectric La: HfO_2 capacitors. *Appl. Phys. Lett.* **112**, 222901 (2018).

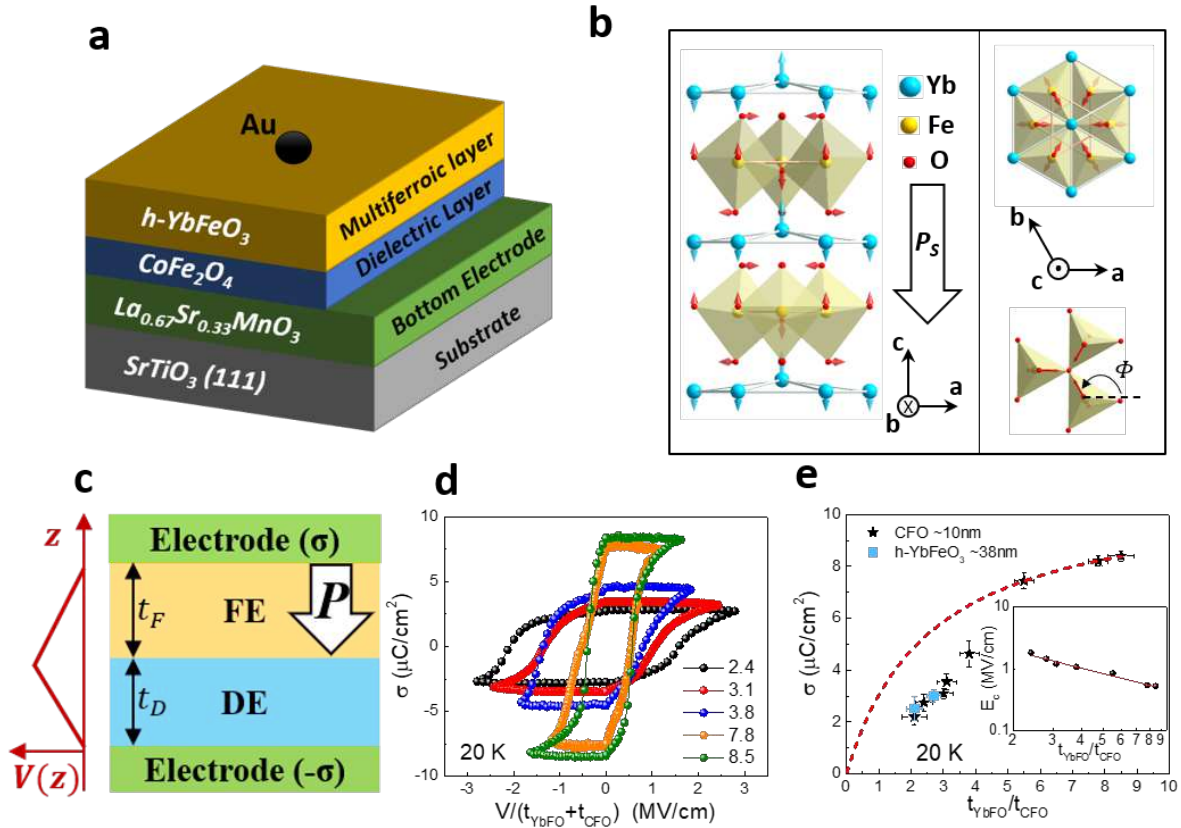


Fig.1 **a)** Schematic diagram of $h\text{-YbFeO}_3/\text{CFO}/\text{LSMO}/\text{STO}$ (111) heterostructure. **b)** Ferroelectric order in $h\text{-YbFeO}_3$. The side and top views of the unit cell show the distribution of tilted FeO_5 bipyramids in the unit cell. The arrows from the atoms indicate the atomic displacement pattern of the primary non-polar K_3 structural distortion which occurs below $T_c \approx 1000$ K. **c)** Schematic diagram for the FE/DE bilayer and electrostatic potential $V(z)$. **d)** $\sigma - E$ loops with various $t_{\text{YbFO}}/t_{\text{CFO}}$ at 20 K. **e)** Remnant polarization σ_r as a function of $t_{\text{YbFO}}/t_{\text{CFO}}$ at 20 K. The black stars represent that the films with various $h\text{-YbFeO}_3$ thickness and fixed CFO thickness ($\sim 10\text{nm}$). For the blue squares, we fixed $h\text{-YbFeO}_3$ thickness (~ 38 nm) and changed the CFO thickness to 14 nm and 18 nm, respectively. Inset: the $t_{\text{YbFO}}/t_{\text{CFO}}$ dependent coercive field E_c .

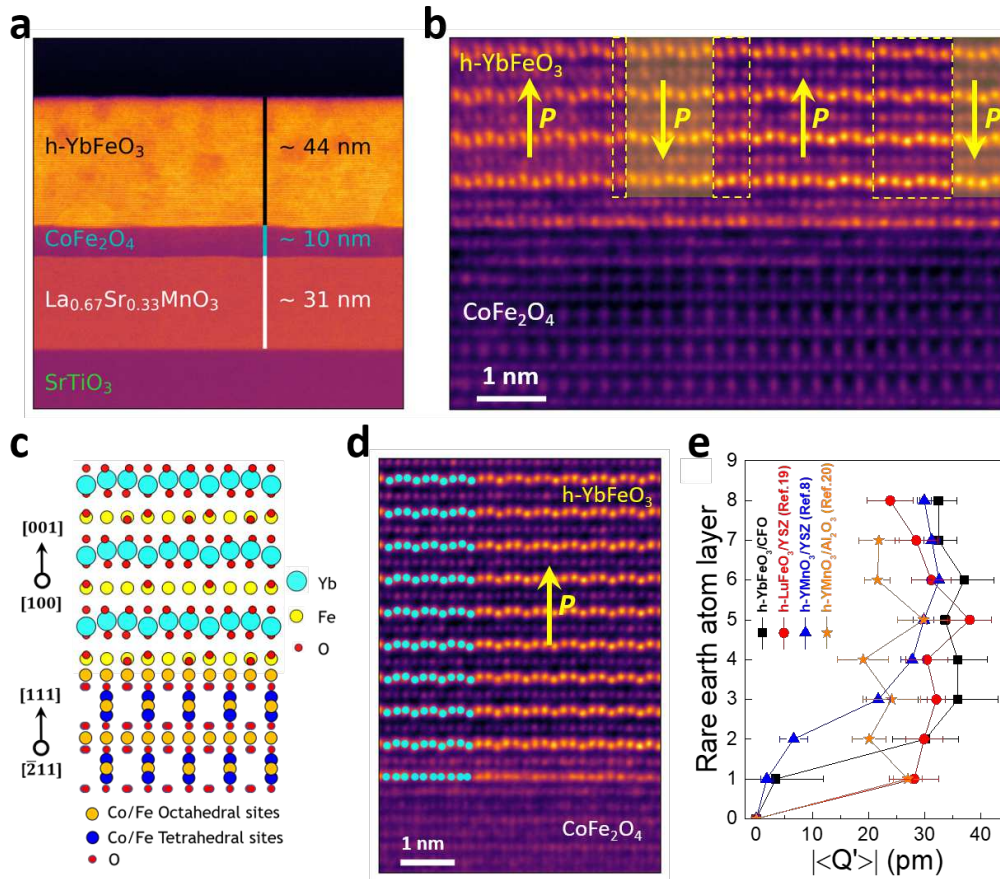


Fig.2 a) A wide field -of -view HAADF-STEM image showing the h-YbFeO₃/CFO/LSMO/STO (111) heterostructure. **b)** Atomic resolution HAADF-STEM image showing the interface between the h-YbFeO₃ film and the CFO dielectric layer. The Yb atoms (brightest ones) show periodic arrangement with “two-up-one-down” and “two-down-one-up” indicating the FE polarization pointing up and down, respectively. The domain walls are marked by dashed-line boxes, and the multidomain states associated with different FE polarization direction are labeled by the arrows and shadow. **c)** Atomic model for the h-YbFeO₃/CFO interface describing the epitaxial relationship between h-YbFeO₃ layer and CFO layer. **d)** Atomic resolution HAADF-STEM image showing the h-YbFeO₃/CFO interface with FE polarization in h-YbFeO₃ film pointing up. Yb atoms (brightest) are labeled in part of the image (cyan colored dots). **e)** Influence of the substrate-film interface on the improper ferroelectricity. Averaged displacement $|\langle Q' \rangle|$ for each rare earth atomic row from the substrates or buffer layer shows saturation within 4 rare earth atom layers (two unit cells). Black squares correspond to the data obtained from the HAADF-STEM image shown in **d**, the other three are obtained from the literature.

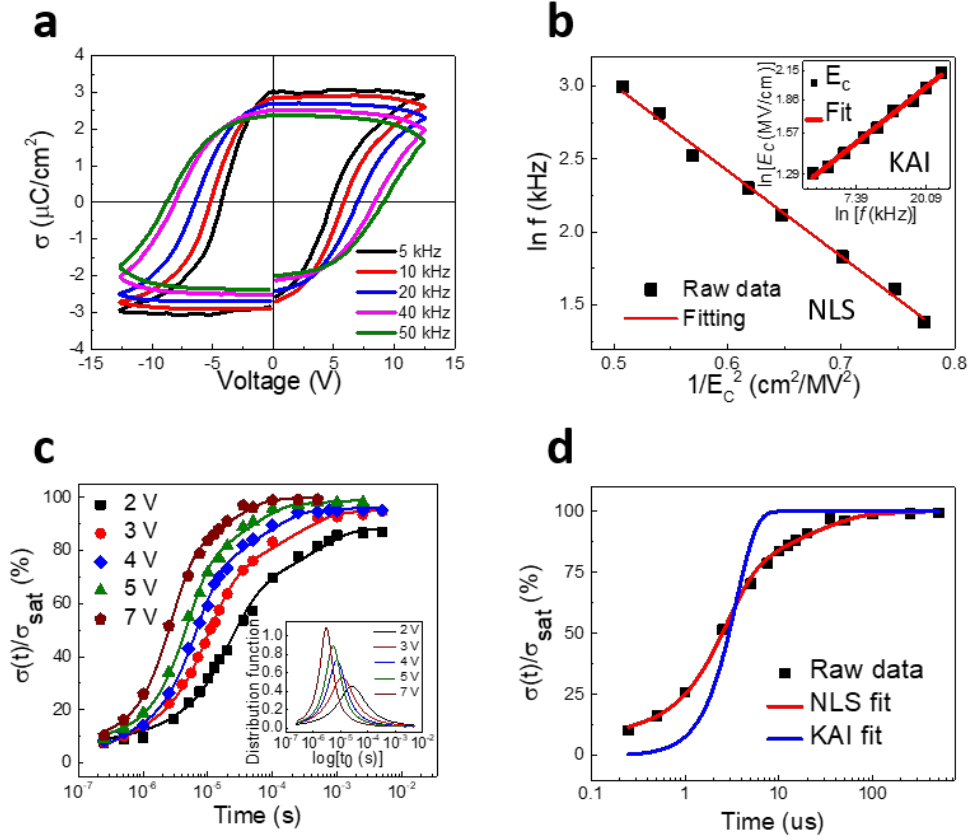


Fig.3 a) Frequency dependent $\sigma - V$ loops for the sample of $t_{YbFO}/t_{CFO} \sim 3.1$ at room temperature. **b)** Frequency dependent coercive field fitted by Du-Chen model. Inset: Fitting by the Ishibashi-Orihara model. **c)** Time (t)-dependent switched polarization under various external voltages. Inset: distribution function for the various external voltages. **d)** Time dependence of the switched area for the 7 V bias fitted by the KAI model and the NLS model.

Figures

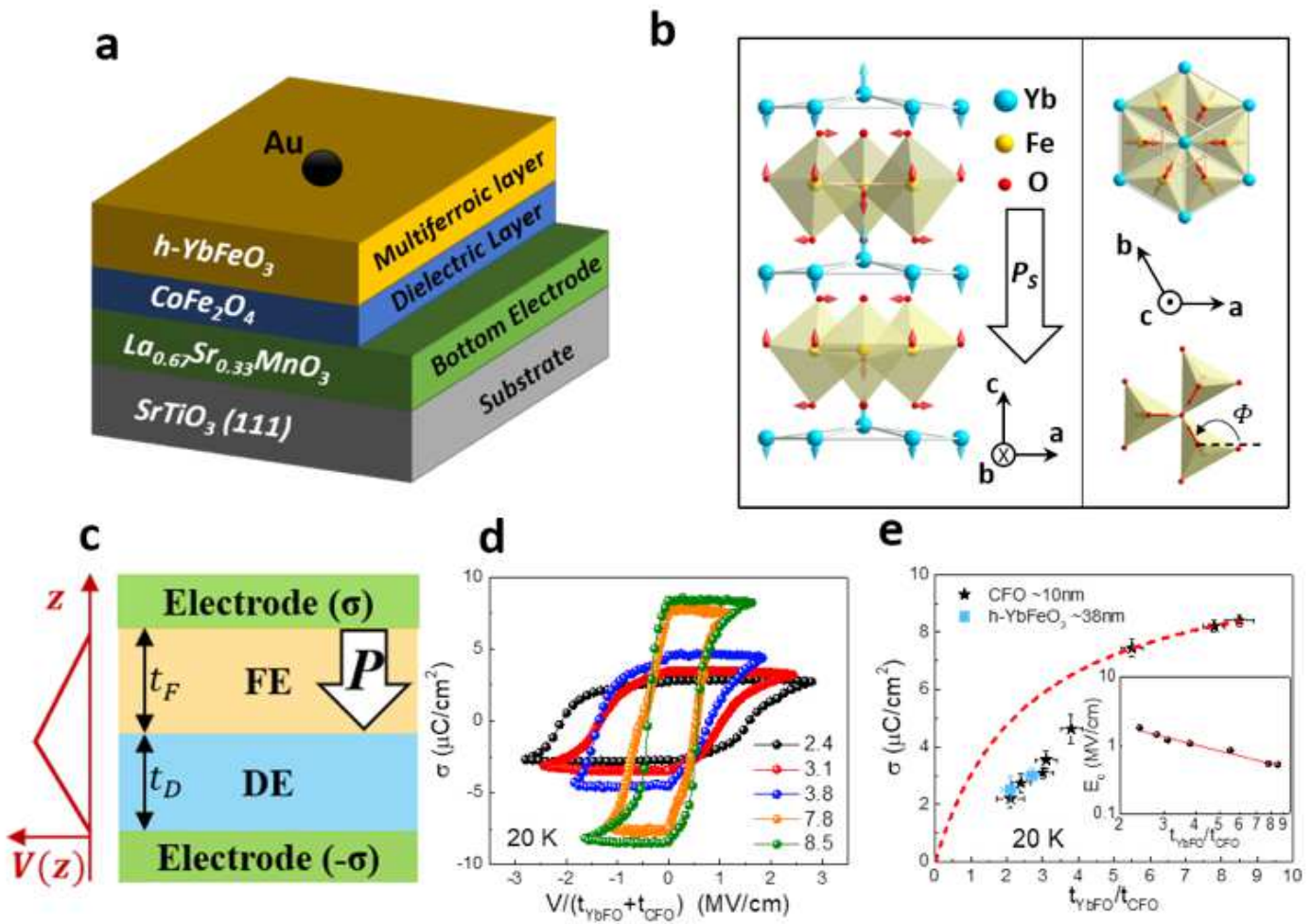


Figure 1

a) Schematic diagram of h-YbFeO₃/CFO/LSMO/STO (111) heterostructure. b) Ferroelectric order in h-YbFeO₃. The side and top views of the unit cell show the distribution of tilted FeO₅ bipyramids in the unit cell. The arrows from the atoms indicate the atomic displacement pattern of the primary non-polar K3 structural distortion which occurs below TC ≈ 1000 K. c) Schematic diagram for the FE/DE bilayer and electrostatic potential V(z). d) $\sigma - E$ loops with various $t_{\text{YbFO}}/t_{\text{CFO}}$ at 20 K. e) Remnant polarization or as a function of $t_{\text{YbFO}}/t_{\text{CFO}}$ at 20 K. The black stars represent that the films with various h-YbFeO₃ thickness and fixed CFO thickness (~10nm). For the blue squares, we fixed h-YbFeO₃ thickness (~38 nm) and changed the CFO thickness to 14 nm and 18 nm, respectively. Inset: the $t_{\text{YbFO}}/t_{\text{CFO}}$ dependent coercive field E_c .

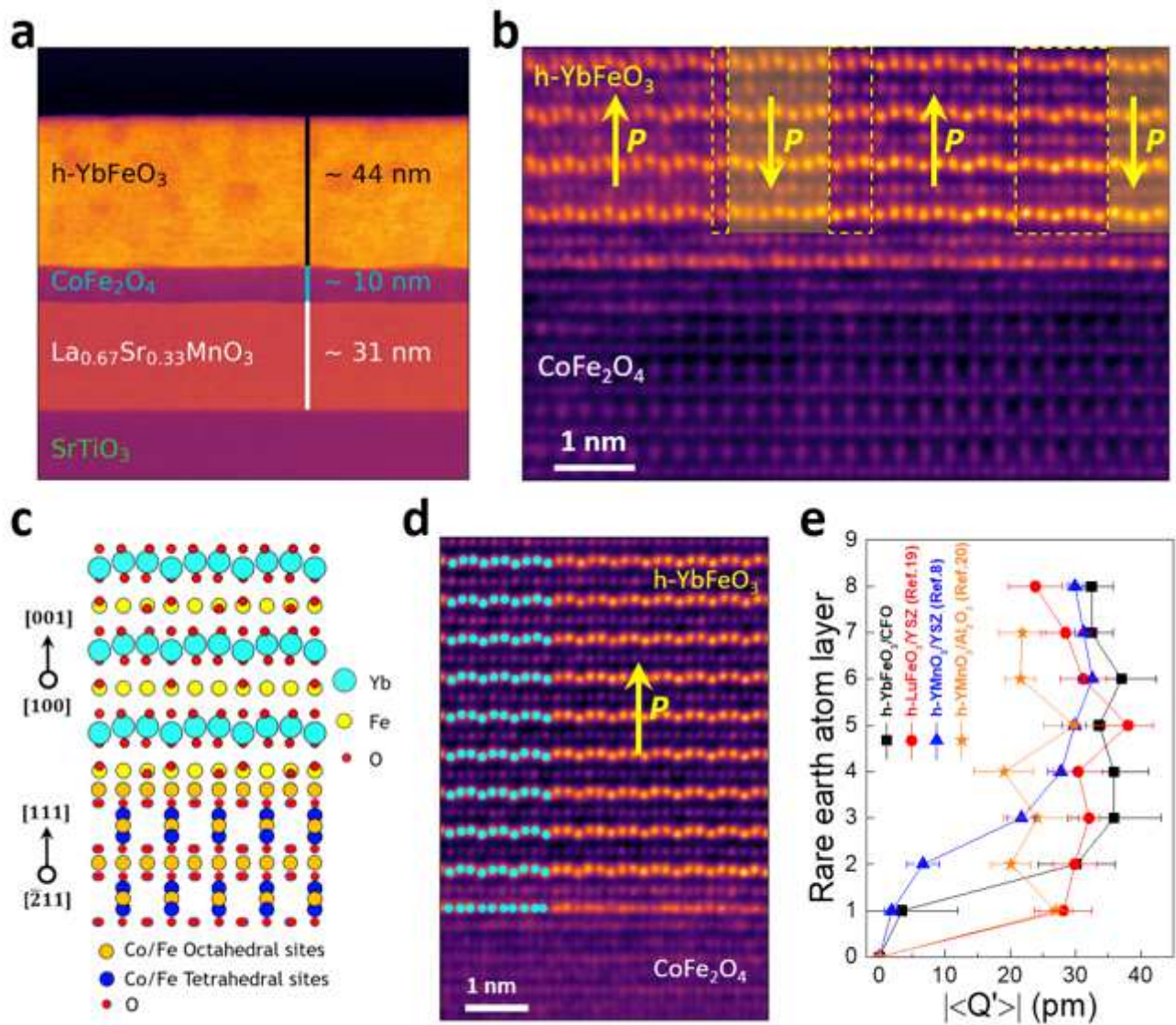


Figure 2

a) A wide field -of -view HAADF-STEM image showing the h-YbFeO₃/CFO/LSMO/STO (111) heterostructure. b) Atomic resolution HAADF-STEM image showing the interface between the h-YbFeO₃ film and the CFO dielectric layer. The Yb atoms (brightest ones) show periodic arrangement with “two-up-one-down” and “two-down-one-up” indicating the FE polarization pointing up and down, respectively. The domain walls are marked by dashed-line boxes, and the multidomain states associated with different FE polarization direction are labeled by the arrows and shadow. c) Atomic model for the h-YbFeO₃/CFO interface describing the epitaxial relationship between h-YbFeO₃ layer and CFO layer. d) Atomic resolution HAADF-STEM image showing the h-YbFeO₃/CFO interface with FE polarization in h-YbFeO₃ film pointing up. Yb atoms (brightest) are labeled in part of the image (cyan colored dots). e) Influence of the substrate-film interface on the improper ferroelectricity. Averaged displacement $|\langle Q' \rangle|$ for each rare earth atomic row from the substrates or buffer layer shows saturation within 4 rare earth atom layers

(two unit cells). Black squares correspond to the data obtained from the HAADF-STEM image shown in d, the other three are obtained from the literature.

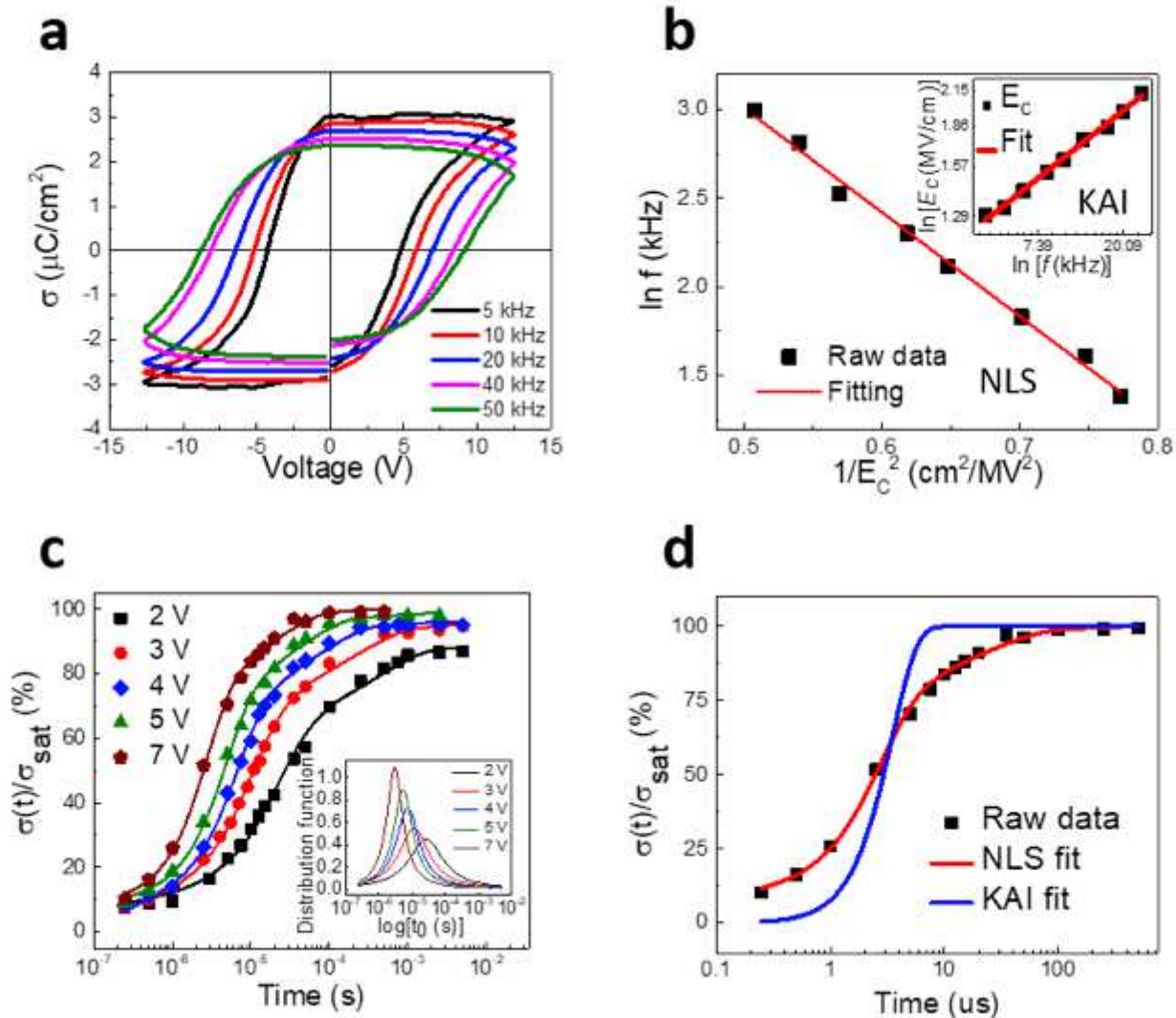


Figure 3

a) Frequency dependent σ - V loops for the sample of tYbFO/tCFO ~ 3.1 at room temperature. b) Frequency dependent coercive field fitted by Du-Chen model. Inset: Fitting by the Ishibashi-Orihara model. c) Time (t)-dependent switched polarization under various external voltages. Inset: distribution function for the various external voltages. d) Time dependence of the switched area for the 7 V bias fitted by the KAI model and the NLS model.

Supplementary Files

This is a list of supplementary files associated with this preprint. Click to download.

- [SI Absence of critical thickness in improper ferroelectric.docx](#)